Equiaxed dendritic growth in nearly isothermal conditions: A study combining in situ and real-time experiment with large-scale phase-field simulation

Tongzhao Gong, Yun Chen, Shanshan Li, Yanfei Cao, Liyuan Hou, Dianzhong Li, Xing-Qiu Chen, Henri Nguyen-Thi, Guillaume Reinhart

Equiaxed dendritic growth in nearly isothermal conditions: A study combining in situ and real-time experiment with large-scale phase-field simulation

Tongzhao Gong [a, b], Yun Chen [a *], Shanshan Li [a, b], Yanfei Cao [a], Liyuan Hou [c], Dianzhong Li [a], Xing-Qiu Chen [a], Guillaume Reinhart [d], Henri Nguyen-Thi [d]

[a] *Shenyang National Laboratory for Materials Science, Institute of Metal Research, Chinese Academy of Sciences, Shenyang 10016, P. R. China*

[b] *School of Materials Science and Engineering, University of Science and Technology of China, Hefei 230026, P. R. China*

[c] *Baotou Rare Earth R&D Center, Chinese Academy of Sciences , Baotou 014000, P. R. China*

[d] *Aix Marseille Univ, Université de Toulon, CNRS, IM2NP, Marseille, France*

Abstract: The equiaxed dendritic growth of Al-Cu alloys in nearly isothermal temperature field under continuous cooling condition is studied using in situ and real-time observation of experiments by synchrotron X-ray radiography and large-scale quantitative two-dimensional (2D) phase-field (PF) simulations. It is revealed that the equiaxed dendritic morphology and the secondary dendritic arm spacing (SDAS) in the 2D PF simulations are in a reasonable agreement with the experimental data. Increasing the cooling rates results in a smaller SDAS, as predicted by the analytical Kattamis-Flemings model. The transformation kinetics of solid fraction can be described by the Johnson-Mehl-Avrami-Kologoromov (JMAK) theory, but quantitative differences between the experiments and 2D PF simulations are significant. The maximum solute concentration C_{max} in liquid is approximately equal to the equilibrium concentration, which depends on the undercooling rather than the cooling rate. But the minimum solute concentration C_{min} in solid decreases with the cooling rate, thus leading to a larger segregation ratio $S_R = C_{max}/C_{min}$. Moreover, the liquid gravity-driven natural convection is considered in simulations. The liquid flow slightly increases the SDAS but has no apparent effect on solid fraction, and the

*Corresponding author. Tel: +86 24 8397 0106; Fax: +86 24 8397 0097.
E-mail address: chenyun@imr.ac.cn (Y. Chen).

segregation ratio is slightly reduced by the liquid convection, which could be attributed to the almost same C_{max} and enlarged C_{min}.

Keywords: equiaxed dendritic growth; polycrystalline solidification; phase-field method; large-scale simulation; synchrotron X-ray radiography.

1. Introduction

The equiaxed dendrite is one of the most common microstructures formed during the solidification process of materials, and its morphology, size, and composition distribution are critical to mechanical properties of castings. A comprehensive and in-depth understanding of equiaxed dendritic growth is of vital importance to control the casting processing for optimizing the quality of final products [1, 2]. Many theoretical progresses have been gained on the steady-state growth of a dendrite growing freely during solidification of pure substances and alloys [3-6], even with considering the influence of melt convection [7-11]. Meanwhile, amounts of solidification experiments of transparent organic alloys [12, 13] were performed to validate these theories. However, exact prediction of the complex pattern formation during solidification is still a big challenge currently. This is because the transport of heat and mass, the melt convection, the crystal morphology, and the interaction among grains are too complex and highly nonlinear to be treated analytically.

The state-of-the-art numerical techniques, such as the quantitative phase-field (PF) method [14], accompanied with the advanced in situ and real-time observation of solidification experiments by synchrotron X-ray radiography [15], have become powerful tools to investigate the microstructure evolution and the related nonlinear physics of metallic alloys during solidification. By means of synchrotron X-ray radiography, Bogno et al. [16] and Becker et al. [17] respectively studied the equiaxed dendritic growth of Al-10 wt.% Cu alloys and Al-24 at.% Ge alloys under the continuous cooling condition, and they found that equiaxed dendrite development was characterized by two successive growth regimes, namely the free growth and impinged growth, which were well reproduced in several recent quantitative PF

simulations by Chen et al. [18], Qi et al. [19] and Boukellal et al. [20]. However, those simulations were limited to a very small computational domain and consider only the cases of one or two grains because of the low computational efficiency of the quantitative PF simulations. It is thus time to unveil the collective behaviors of a large number of grains during solidification for metallic materials. Besides, the XRMON-SOL experiment [21] was carried out by Murphy et al. to investigate the equiaxed dendrite growth under the influence of solutal interactions, then the XRMON-SOL experiment were modelled using a recently developed 3D mesoscopic envelope method [22, 23], which provided a feasible scheme for large-scale simulation of solidification microstructure evolution. However, the branched dendritic structure could not be obtained by this method and therefore it is still necessary to perform quantitative PF simulations to accurately predict pattern formation and evolution of materials during solidification.

In the last few years, the quantitative large-scale PF simulations have been achieved [24-26], due to the rapid development of numerical methods and computer hardware. In this paper, the large-scale quantitative 2D PF simulations are carried out using the fast simulation schemes proposed in our previous study [25], to reproduce the in situ and real-time observed polycrystalline solidification experiments of Al-4 wt.% Cu alloys under the continuous cooling condition. The simulated equiaxed dendritic growth is directly compared with the synchrotron X-ray radiography monitoring data, and the effects of the cooling rate and the liquid gravity-driven natural convection on the equiaxed dendritic growth during solidification are also discussed. The aim of the present work is to realize the large-scale quantitative PF simulation with the number of grains and computational domain comparable to the real solidification experiment, and the fluid dynamics equations are extremely difficult to solve efficiently for such a large-scale quantitative 3D PF simulation. Based on these two points, it is reasonable and necessary to carry out the 2D large-scale PF simulation that is relatively easier to implement as a first step before more realistic but challenging 3D simulations.

2. In situ and real-time observation of solidification experiments

The in situ and real-time observation of solidification experiments of Al-4 wt.% Cu alloys were implemented at ID19 beamline of the European Synchrotron Radiation Facility (ESRF) in Grenoble (France), and the detailed description of the experiment set-up and procedure was given in ref. [16]. The thin samples (40 mm × 6 mm × 0.2 mm) of Al-4 wt.% Cu alloys were set vertically in a Bridgman furnace, and two heating elements were placed on the top and bottom of the sample to melt the sample in nearly isothermal conditions. During the experiment, the sample was first melted and maintained to a temperature above the liquidus temperature for several hours to homogenize the solute composition in liquid. Then solidification was triggered by simultaneously applying the same cooling rate on both heating elements. A 10-μm-camera optics was chosen to obtain a good compromise between a large field of view (5 mm × 12 mm) and a sufficient spatial resolution (pixel size 7.46 μm).

The time evolution of equiaxed dendritic microstructure of Al-4 wt.% Cu alloys in the solidification experiment at various cooling rates is shown in Fig. 1~~Fig. 1~~, in which the Al-rich solid crystals appear in white and the Cu-rich liquid is in darker grey after a special image processing [27] to improve the quality of images. As seen in Fig. 1~~Fig. 1~~, a great number of grains nucleated and grew from the melt during the continuous cooling, and then the equiaxed grains rapidly interacted with neighbors owing to the spatial constraint. A comprehensive study of the equiaxed dendritic growth with the same experimental procedure but on Al-10 wt.% Cu alloys had been reported [16], and the main conclusion was that the equiaxed dendritic growth experienced two regimes: an accelerating regime corresponding to the stage when a growing dendrite arm was isolated from its neighbors, and a decelerating regime where the solute interaction had a suppression effect. Furthermore, from Fig. 1~~Fig. 1~~ it could also be seen that with the cooling rate increasing, the number of grains in the experiments will increase and the secondary dendritic arm spacing (SDAS) will decrease, thus leading to a refined equiaxed dendritic microstructure.

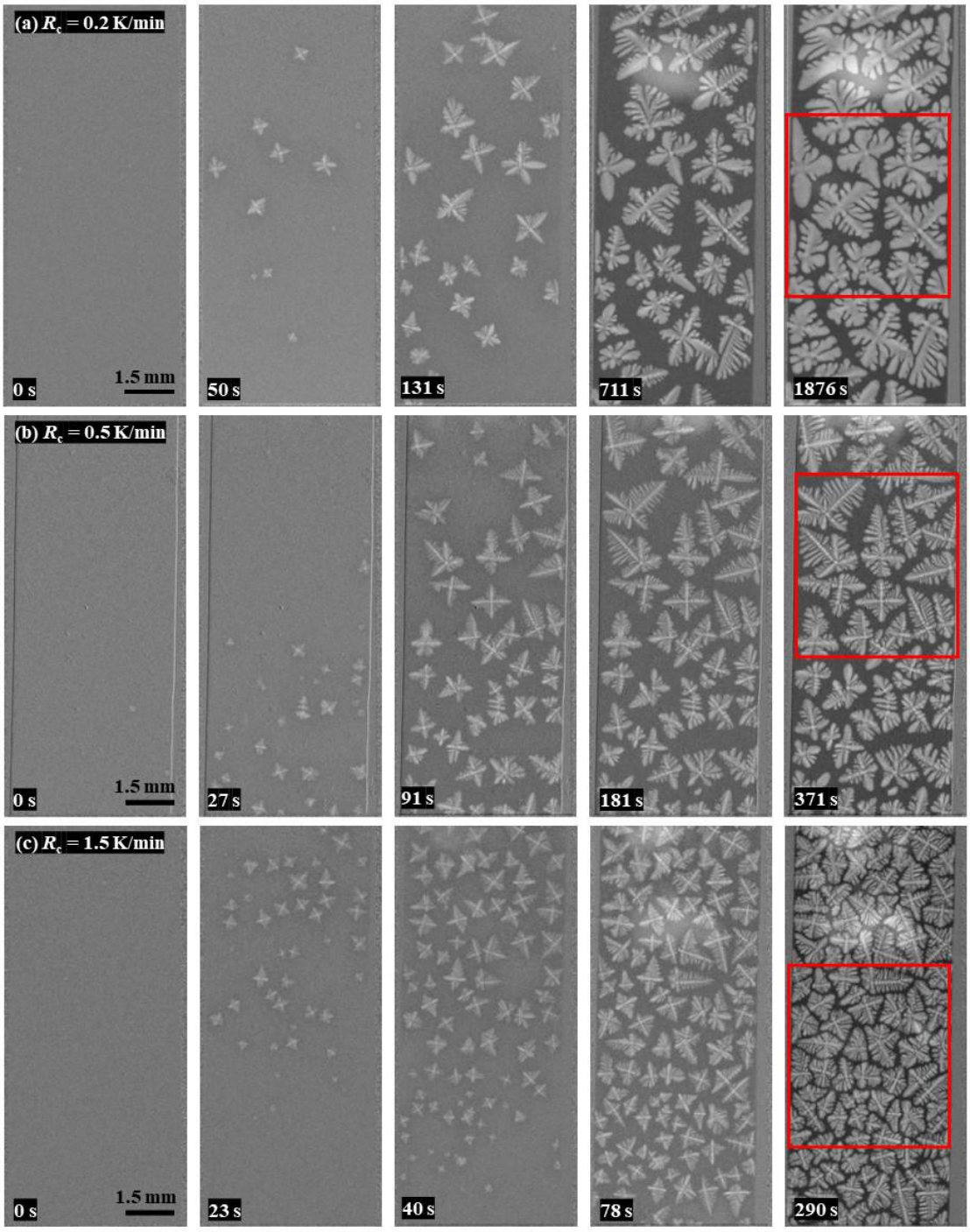

Fig. 1. Sequence of in situ radiographs showing the equiaxed dendritic microstructure evolution in the solidification experiments of Al-4 wt.% Cu alloys at various cooling rates, R_c. (**a**) E1: R_c = 0.2 K/min; (**b**) E2: R_c = 0.5 K/min; (**c**) E3: R_c = 1.5 K/min.

It should be noticed that the experiment E2 (Fig. 1~~Fig. 1~~(b)) has been analyzed in our previous study [18]. However, compared with ref. [18], the 2D simulations presented in this paper have several improvements. The computational domain size

(4233 μm × 7408 μm) in ref. [18] was comparable to the sample size shown in Fig. 1~~Fig. 1~~(b), but only one single isolated equiaxed crystal and two grains growing opposite each other were considered, which was not able to unveil the collective behavior of multi-grain growth. Moreover, the gravity-driven natural convection was not considered in our previous PF simulation [18]. Therefore, the experiment (E2), accompanied by other two experiments (E1 and E3) with different cooling rates of Al-4 wt.% Cu alloy which is suitable for PF simulations owing to the low composition, is reused in the present work to give a clear picture of multi-grain growth during solidification. The reason why the PF model is only suitable for dilute alloys with a low solute concentration is that the Gibbs free energies of both liquid and solid phases are calculated using the regular solution model, in which the high order terms in the excess free energy are ignored [28].

3. Phase-field model and numerical implementations

3.1 Phase-field model

The quantitative PF model presented in ref. [28] is adopted to model solidification of dilute binary alloys under continuous cooling condition, and the quantitative capability of this model to reproduce the time evolution of microstructure during alloy solidification has been demonstrated in many previous studies [20, 29-31]. The governing equations of the phase field ϕ and the rescaled solute concentration U are respectively given as

$$\left(1+\frac{R_c t}{|m|C_0}\right)\tau(\mathbf{n})\frac{\partial\phi}{\partial t}=\nabla\cdot\left[W(\mathbf{n})^2\nabla\phi\right]+\sum_{i=x,y}\partial_i\left[|\nabla\phi|^2 W(\mathbf{n})\frac{\partial W(\mathbf{n})}{\partial(\partial_i\phi)}\right] +\phi-\phi^3-\lambda\left[U-\frac{R_c t}{(1-k)|m|C_0}\right]\left(1-\phi^2\right)^2 \tag{1}$$

$$\frac{(1+k)-(1-k)\phi}{2}\frac{\partial U}{\partial t}=\nabla\cdot\left\{D_L\left[\frac{1-\phi}{2}+\frac{k(1+\phi)D_S}{2D_L}\right]\nabla U\right\} +\nabla\cdot\left\{\frac{W_0\left[1+(1-k)U\right]}{2\sqrt{2}}\frac{\partial\phi}{\partial t}\frac{\nabla\phi}{|\nabla\phi|}\right\}+\frac{1+(1-k)U}{2}\frac{\partial\phi}{\partial t} \tag{2}$$

with

$$U = \frac{2C/C_0 - \left[(1+k) - (1-k)\phi\right]}{(1-k)\left[(1+k) - (1-k)\phi\right]} \tag{3}$$

where C is the local solute concentration, C_0 is the initial concentration, k is the solute partition coefficient, R_c is the cooling rate, and m is the liquidus slope. The solid and liquid phases are represented by $\phi = +1$ and $\phi = -1$, respectively. The spatial length and time are rescaled respectively by the interface width W_0 and relaxation time τ_0, and therefore the dimensionless value for the solute diffusion coefficient in liquid is

$$\tilde{D} = \frac{D_L \tau_0}{W_0^2} = a_1 a_2 \frac{W_0}{d_0} \tag{4}$$

where $d_0 = \Gamma/[|m|C_0(1-k)]$ is the chemical capillary length with Γ the Gibbs-Thomson coefficient, $a_1 = 5\sqrt{2}/8$ and $a_2 = 47/75$ [28]. It should be noted that for Al-Cu alloys, although the solute diffusion in solid is much slower than that in liquid (the solid diffusivity is about 3 orders of magnitude smaller than the liquid diffusivity), a small solid diffusivity can be taken into account, as indicted in the original derivation of the model in ref. [32]. And this way to model the real solute diffusion in solid was also employed in our previous study [29], in which D_S in Eq. (2)~~(2)~~ is the solute diffusion coefficient in solid. The coupling coefficient λ in Eq. (1)~~(1)~~ is given as $\lambda = a_1 W_0/d_0$. The standard form of the fourfold symmetry of the surface energy anisotropy is considered, and thus $W(\mathbf{n}) = W_0 a_s(\mathbf{n})$ and $\tau(\mathbf{n}) = \tau_0 a_s(\mathbf{n})^2$ where

$$a_s(\mathbf{n}) = 1 - 3\varepsilon_4 + 4\varepsilon_4 \sum_{i=x,y} \frac{(\partial_i \phi)^4}{|\nabla \phi|^4} \tag{5}$$

In order to expedite quantitative large-scale PF simulations, a nonlinear preconditioning [33] of the phase field ϕ is employed to allow coarser grids to be used in the interface layer. The transformed phase field ψ is given as

$$\psi = \tanh\left(\frac{\phi}{\sqrt{2}}\right) \tag{6}$$

And hence the standard PF model (Eqs. (1)~~(1)~~ and (2)~~(2)~~) is transformed into the nonlinearly preconditioned formula, as follows

a mis en form
12 pt, Couleur

a mis en form
12 pt

a mis en form
12 pt

a mis en form
12 pt

$$\left(1+\frac{R_c t}{|m|C_0}\right)\tau_0 a_s^2(\mathbf{n})\frac{\partial\psi}{\partial t}=W_0^2 a_s^2(\mathbf{n})\left[\nabla^2\psi-\sqrt{2}\tanh\left(\frac{\psi}{\sqrt{2}}\right)|\nabla\psi|^2\right]$$
$$+\sum_{i=x,y}W_0^2\partial_i\left[|\nabla\psi|^2 a_s(\mathbf{n})\frac{\partial a_s(\mathbf{n})}{\partial(\partial_i\psi)}\right]+\sqrt{2}\tanh\left(\frac{\psi}{\sqrt{2}}\right) \quad (7)$$
$$-\sqrt{2}\lambda\left[1-\tanh^2\left(\frac{\psi}{\sqrt{2}}\right)\right]\left[U-\frac{R_c t}{(1-k)|m|C_0}\right]$$

$$\frac{(1+k)-(1-k)\tanh\left(\frac{\psi}{\sqrt{2}}\right)}{2}\frac{\partial U}{\partial t}$$
$$=\nabla\cdot\left\{D_L\left[\frac{1-\phi}{2}+\frac{k(1+\phi)D_S}{2D_L}\right]\nabla U+\frac{1}{2}W_0\left[1+(1-k)U\right]\frac{1-\tanh^2\left(\frac{\psi}{\sqrt{2}}\right)}{2}\frac{\partial\psi}{\partial t}\frac{\nabla\psi}{|\nabla\psi|}\right\} \quad (8)$$
$$+\frac{1+(1-k)U}{2}\frac{1-\tanh^2\left(\frac{\psi}{\sqrt{2}}\right)}{\sqrt{2}}\frac{\partial\psi}{\partial t}$$

The numerical accuracy and efficiency of the preconditioned PF formula has been examined previously [25]. In the PF simulations, as the nucleation undercoolings of grains are neglected, all the grains nucleated simultaneously at the beginning of solidification (at the liquidus temperature), and the number, site, and orientation of the grains in simulations are measured directly from the radiography images in Fig. 1~~Fig. 1~~ for various cooling rates.

3.2 Numerical implementations

The parallel adaptive finite element method, with multiple processors using distributed memory based on MPI protocol, is employed to solve the preconditioned PF model. Numerical implementations are realized by the open source deal.II library [34], and the adaptive mesh refinement/coarsening is achieved through a simple but efficient approach [25]. The front-tracking method [25] is also used to capture crystallographic orientations to improve computing efficiency dramatically. The computational domain size is 5.0 mm × 5.6 mm (marked by the red boxes in Fig. 1~~Fig. 1~~), which is comparable with the spatial scale of the sample in the solidification experiment.

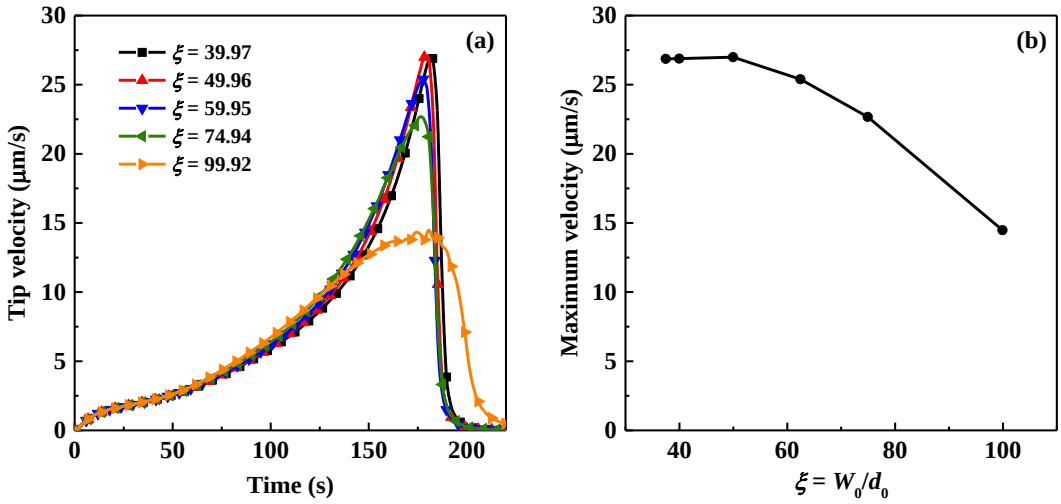

Fig. 2. The convergence test of the interface width parameter, $\xi = W_0/d_0$, used in the quantitative 2D PF simulation of the Al-4 wt.% Cu alloy at the cooling rate R_c = 1.5 K/min. (**a**) Variation of the tip velocity with solidification time; (**b**) Variation of the maximum tip velocity with ξ.

The interface width parameter, $\xi = W_0/d_0$, was determined according to the convergence test (Fig. 2~~Fig. 2~~), which was carried out for a single equiaxed dendrite of the Al-4 wt.% Cu alloy at the cooling rate R_c = 1.5 K/min. The computational domain size for the convergence test was 3 mm × 3 mm, which was sufficient for the largest dendrite in the solidification experiments shown in Fig. 1~~Fig. 1~~. It could be found that with ξ decreasing, the tip velocity curves gradually converge (Fig. 2~~Fig. 2~~(a)), and the maximum velocity is almost constant once $\xi \leq 49.96$ (Fig. 2~~Fig. 2~~(b)). Therefore, ξ = 49.96 was chosen in the present work to obtain a reasonable compromise between the quantitative simulated results and the computational efficiency. Thus, using this interface width parameter, the corresponding simulation domain size in dimensionless is 5000 × 5600. It should be noticed that for the other cases with lower cooling rates, the choice of ξ = 49.96 is small enough owing to the relatively lower crystal growth rate. The material and numerical parameters are listed in Table 1~~Table 1~~.

All the simulations were implemented on a supercomputer with two AMD® EPYC 7452 (2.35 GHz) CPUs and 256 GB memory at each computing node. For the

case with the largest number of grains (46 grains and R_c = 1.5 K/min), it took about 60 hours to finish the 2D PF simulation using 128 cores until the solid fraction got close to that in the last radiography image (f_S = 0.6) recorded in the corresponding solidification experiment. For the case with R_c = 0.2 K/min, although the number of grains was reduced to 15, the computing time until the solid fraction reached 0.525 was about 150 hours using 128 cores owing to the much slower cooling rate.

Table 1. Material and numerical parameters used in the present 2D PF simulations.

Symbol	Meaning	Value
k	solute partition coefficient	0.14 [27]
T_L	liquids temperature	920 K [35]
D_L	solute diffusion coefficient in liquid	2.42×10−5 cm^2/s [36, 37]
D_S	solute diffusion coefficient in solid	1.15×10^{-8} cm^2/s [36]
Γ	Gibbs-Thomson coefficient	2.41×10^{-5} cm·K [38]
m	liquidus slope	−3.5 K/wt.%
ε_4	surface energy anisotropy strength	0.0106 [39]
R_c	cooling rate	0.2, 0.5, 1.5 K/min
C_0	sample global concentration	4 wt.% Cu
ξ	interface width parameter	49.96
$(\Delta x)_{min}$	grid size in the interface layer	1.0 μm
Δt	time step	1.14×10^{-3} s

4. Results and discussions

4.1 Equiaxed dendritic morphology

The equiaxed dendritic microstructure in a local domain selected from the solidification experiments at various cooling rates (E1 to E3) and the corresponding 2D PF simulations (S1 to S3) are shown in Fig. 3~~Fig. 3~~. Overall, the simulated equiaxed dendritic microstructures are in a reasonably good agreement with the radiography images, except that the primary dendritic arms in the simulations are

generally much thicker than those in the experiments. The difference in the thickness of the primary dendritic arms could be attributed to the different equiaxed dendritic growth dynamics. As indicated in our previous study [40], the tip velocity of the primary dendritic arm in the 2D PF simulations is 1~2 orders of magnitude slower than that in the 3D PF simulations. In practice, the crystal growth in the experiments is in a 3D space despite of the thin-sample configuration. This can be understood by comparing the typical dendrite tip radius to the sample thickness. Consequently, the crystal growth rate in the 2D PF simulations is much slower than that in the experiments [18], thus leading to a relatively larger tip radius [40]. In addition, a low growth rate allows a long time for solute diffusion, which would make the primary arm stems grow laterally. The differences of dendrite growth between 2D and 3D can also be directly clarified by the recent work by Mirihanage et al. [41], in which a novel image processing algorithm was applied to extract data on dendrite tip curvatures and accompanying solute concentration fields, from a sequence of synchrotron radiogra~~ms~~phy collected in situ during directional solidification of the Al-Cu-Si alloy.

Moreover, the secondary dendritic arms in the simulations are not so developed as those in the experiments, which also arises from the different dynamical behavior of crystal growth in 2D and 3D. Because of the confinement of solute diffusion, the solute boundary layer in 2D is thicker than in 3D [40], which leads to a stronger solutal interaction between neighboring grains in the 2D PF simulations. As a result, the development of secondary dendritic arms in 2D PF simulations is suppressed by the solute interaction more severely, resulting in commonly shorter secondary dendritic arms. In order to quantitatively evaluate the difference of the equiaxed dendritic morphology in the experiments and the 2D PF simulations, the SDAS, λ_2, is measured at the same solid fraction (f_S = 0.5) and the results are given in **Fig. 4**~~**Fig. 4**~~. In both experiments and simulations, λ_2 decreases as the cooling rate increases (**Fig. 4**~~**Fig. 4**~~(a)), which is consistent with the analytical prediction by Kattamis and Flemings who indicated that the λ_2 could be expressed as a power function of the cooling rate, namely $\lambda_2 \sim R_c^n$ with $n = -1/3$ [42]. Furthermore, with the cooling rate

increasing, the distribution range of the λ_2 will be also reduced, which could be easily found from the detailed distribution information of the λ_2 as shown in Fig. 4~~Fig. 4~~(b).

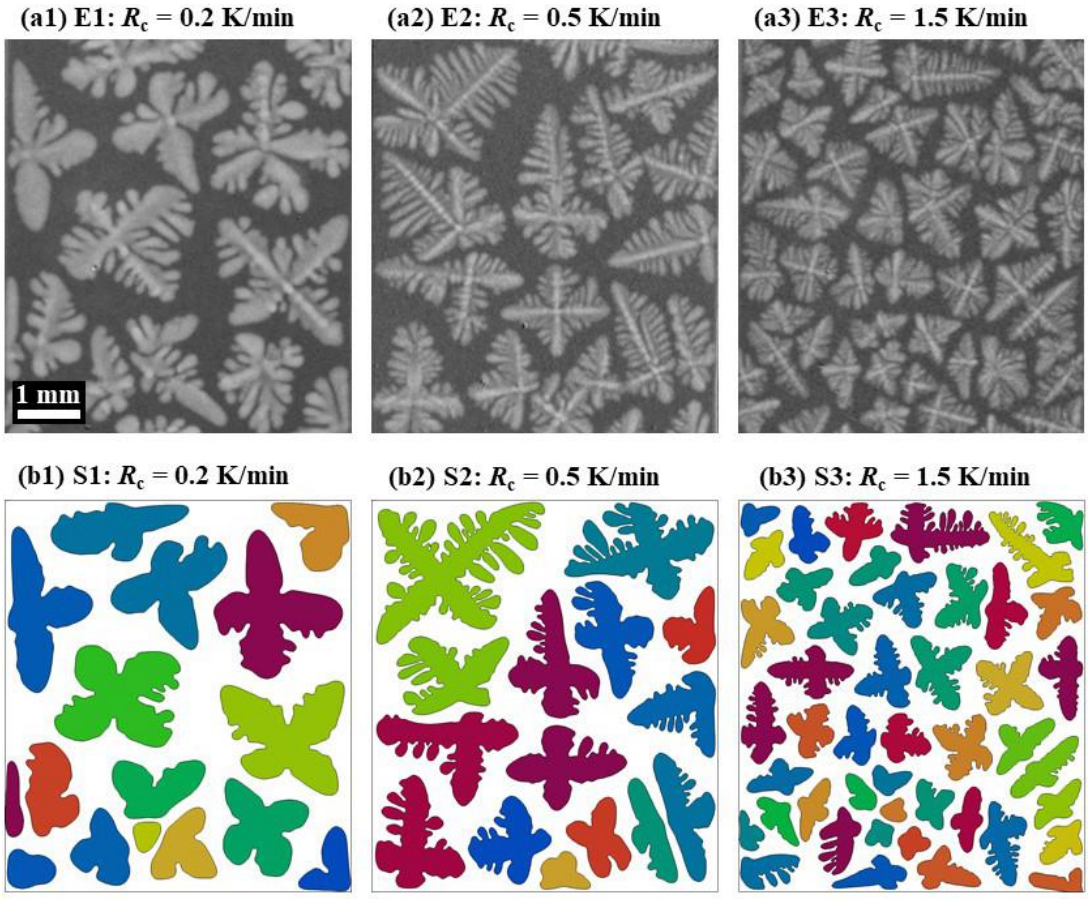

Fig. 3. Equiaxed dendritic morphology in the solidification experiments (E1 to E3 shown in **a1** to **a3**) and the 2D PF simulations (S1 to S3 shown in **b1** to **b3**) at the same solid fraction f_S = 0.5 in local domains marked by the red boxes in Fig. 1~~Fig. 1~~. The colors (b1 to b3) represent the crystal orientations.

Moreover, from the quantitative perspective, the λ_2 in the 2D PF simulations are slightly larger than those in the solidification experiments. The quantitative differences in λ_2 between the experiments and simulations may be attributed to that in simulations it took a relatively longer time to get the same solid fraction than that in experiments (Fig. 5~~Fig. 5~~). Consequently, longer duration enables the secondary dendritic arms in the 2D PF simulations to coarsen more significantly, thus leading a slightly larger λ_2. However, the relative deviations of the λ_2 between the experiments and simulations at R_c = 0.2, 0.5 and 1.5 K/min are about 2%, 12% and 3%,

respectively, so it seems reasonable to consider that the λ_2 in the 2D PF simulations shows a good quantitative agreement with the experimental data.

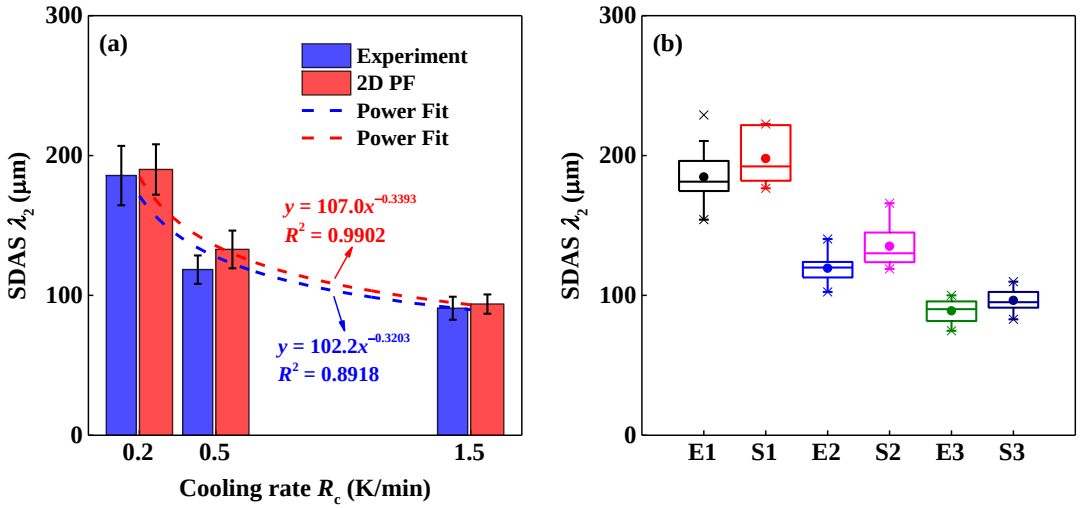

Fig. 4. Comparison of the SDAS, λ_2, between the solidification experiments (E1 to E3) and 2D PF simulations (S1 to S3) at the same solid fraction (f_S = 0.5). (**a**) The average λ_2 at various cooling rates (the error bars represent the standard deviation); (**b**) Box plot of the λ_2 (the cross symbols are the maxima and minima, the filled circles are the means, the whiskers represent the 5 to 95 percentiles, the box top and bottom respectively represent the second and third quartiles, and the lines inside the box represent the medians).

4.2 Solid fraction

The solid fraction, f_S, in the solidification experiments and the 2D PF simulations is plotted and compared quantitatively in Fig. 5~~Fig. 5~~. At the early solidification stage when grains are isolated from each other, the crystal growth rate increases with the undercooling, and therefore the f_S increases gradually (Fig. 5~~Fig. 5~~(a)) at an ever-increasing rate (Fig. 5~~Fig. 5~~(b)) in both experiments and simulations. Then, the solute interaction between neighboring grains slows the crystal growth, but the solidification still proceeds (e. g., the coarsening of primary and secondary dendritic arms) to make the f_S continue to increase (Fig. 5~~Fig. 5~~(a)), despite of the ever-decreasing variation rate (Fig. 5~~Fig. 5~~(b)). However, there indeed exist significant quantitative differences in the f_S between the experimental data and the

simulated results. At the same time, the f_S and its time derivative, $\Delta f_S/\Delta t$, in the simulations are both lower than those in the experiments. The quantitative differences in the f_S between the experiments and simulations could be mainly attributed to three factors. Firstly, the f_S measured directly from the radiography images, which are 2D projections of the complicated 3D dendritic microstructure, usually overestimates the real solid fraction in a 3D sample. Secondly, the much lower crystal growth rate in 2D PF simulations compared with that in 3D cases [40] results in slower solidification kinetics than the experiments. More importantly, all the grains nucleated simultaneously at the beginning of solidification in PF simulations, and the nucleation undercooling was not taken into consideration. In the real solidification experiments, the grains nucleated at different temperatures due to different nucleation undercoolings. Therefore, the nucleation undercooling which was neglected in the simulations may also play an important role on the difference between the simulations and the experiments.

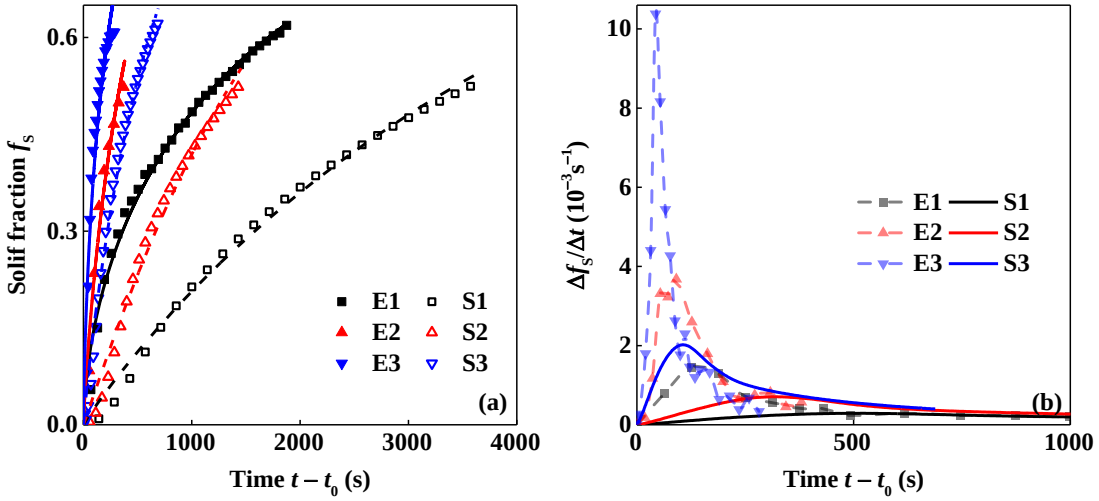

Fig. 5. Comparison of the solid fraction between the solidification experiments (E1 to E3) and the 2D PF simulations (S1 to S3). (**a**) Solid fraction, f_S; (**b**) Variation rate of the solid fraction, $\Delta f_S/\Delta t$. t_0 is the time when the first grain is observed by the naked eye in the radiography images in the experiments. The solid and dashed lines are the fitting curves by the JMAK function for the experimental data and simulated results, respectively.

In general, the curves of the solid fraction in both the solidification experiments and the 2D PF simulations show similar trends (Fig. 5~~Fig. 5~~), which could be fitted well by the Johnson-Mehl-Avrami-Kolmogorov (JMAK) equation [43-45] as

$$f_S = 1 - \exp\left[-(kt)^n\right] \tag{9}$$

where k is the frequency factor, n is the Avrami exponent and t is the solidification time. The general equation for the Avrami exponent is given as

$$n = qd + B \tag{10}$$

where q equals 1 for linear growth (interface controlled) and 1/2 for parabolic growth (diffusion controlled), B is 0 for site saturation nucleation and 1 for continuous nucleation with a constant rate, and d stands for the dimensionality of the growth. The fitting parameters, k and n for both the experimental and simulated data, are plotted in Fig. 6~~Fig. 6~~.

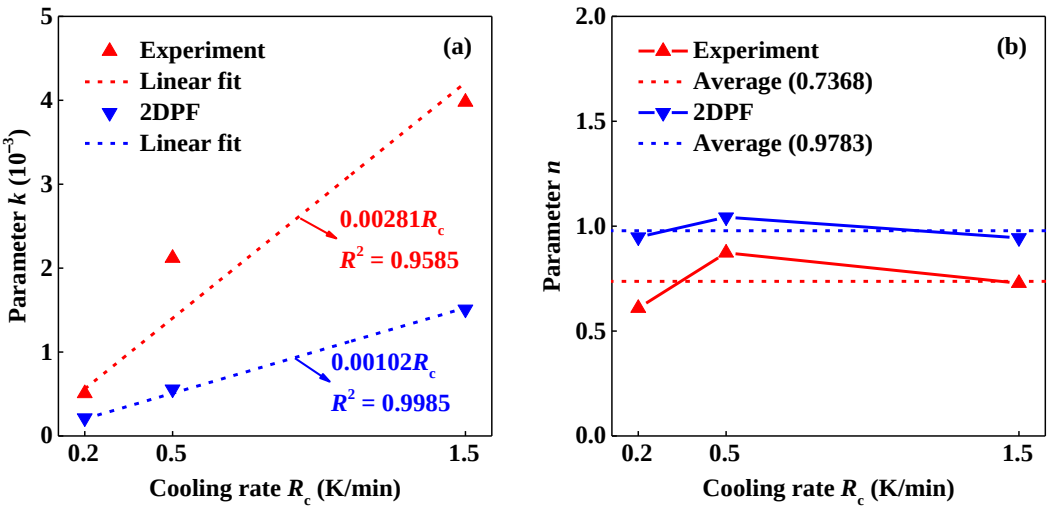

Fig. 6. Plotting of the fitting parameters, k (**a**) and n (**b**), for the solid fraction in the experiments and 2D PF simulations at different cooling rates via the JMAK equation.

In both the solidification experiments and 2D PF simulations, an approximate linear relationship is indicated between the factor k in the JMAK equation (Eq. (9)~~(9)~~) and the cooling rate (Fig. 6~~Fig. 6~~(a)), as $k = \alpha R_c$ with α a positive fitting parameter.

a mis en form
12 pt

And the Avrami exponent n could be considered approximately as a constant (Fig. 6~~Fig. 6~~(b)). As mentioned above, for the 2D PF simulation (d = 2) where the solidification process is diffusion-controlled (q = 1/2) and the nucleation is achieved by artificially setting the number of the pre-existing nuclei (B = 0), the Avrami exponent is $n = qd + B = 1$ that is close to the fitted value (0.9783). However, for the experiments in 3D actually (d = 3) with continuous nucleation (B = 1), the expected Avrami exponent is $n = qd + B = 2.5$ but the fitted value is 0.7368 that is only about 1/3 of the prediction by Eq. (10)~~(10)~~. The significant difference of n between the experimental data and the predicted value could be attributed to that the solid fraction is measured from the 2D radiography images in the experiments, instead of the 3D bulk sample. On the contrary, the 2D PF simulations are able to well describe the transformation kinetics in 2D as the JMAK equation.

a mis en form
12 pt

4.3 Microsegregation

Microsegregation during alloy solidification has always been a concern in materials and metallurgical sciences owing to its influence on the mechanical properties, corrosion resistance of cast products and formation of macrosegregation. Effects of cooling rates on solute microsegregation, including the maximum concentration C_{max} in the interdendritic liquid, the minimum concentration C_{min} in the core of the solid dendrite, and the solute segregation ratio $S_R = C_{max}/C_{min}$, in the 2D PF simulations are shown in Fig. 7~~Fig. 7~~. It could be seen that the cooling rate has no obvious effect on C_{max}, which is almost the same as the equilibrium concentration, $C_L^E = C_0 - \Delta T/m$. For Al-Cu alloys, the solute partition coefficient $k < 1$, which means that the solute is rejected into the liquid phase from the solid phase during solidification. As a result, C_{max} is achieved in the interdendritic liquid around the root of sidebranches. The approximate equality relationship between C_{max} and C_L^E suggests that the interface curvature effect could be neglected safely. Consequently, the maximum solute concentration depends on the applied undercooling, namely the product of the cooling rate and the solidification time $R_c t$, rather than the cooling rate itself, which has also been clarified in our recent study [46]. C_{min} is located at the

center of the solid grain and increases with the undercooling (or the solidification time), but varies much slower than C_{max} owing to the very small solid diffusivity. With a large cooling rate, the diffusion time to get the same undercooling is shortened, thus leading to a lower C_{min} and a larger S_R.

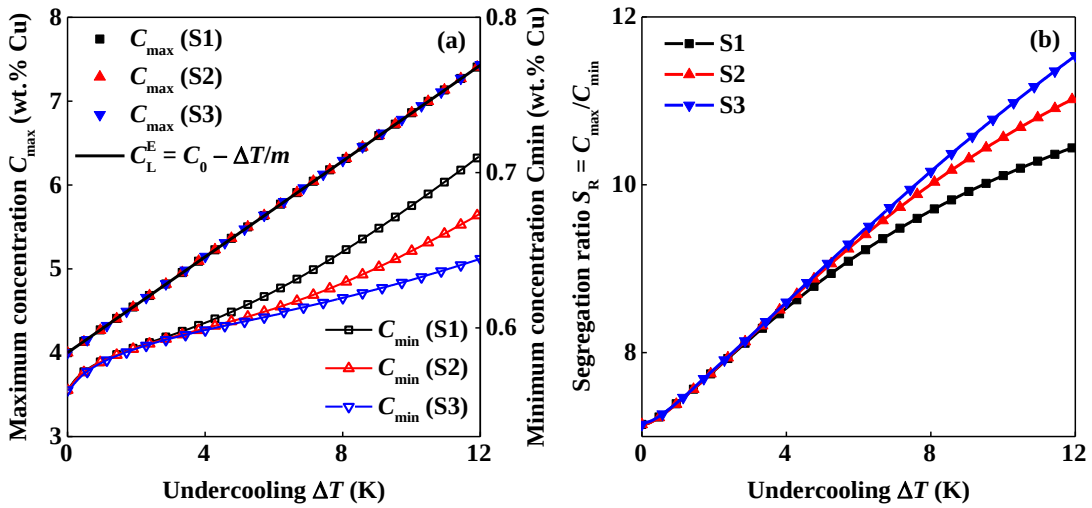

Fig. 7. Effects of cooling rates on solute microsegregation in the 2D PF simulations. (**a**) Maximum and minimum solute concentration, C_{max} and C_{min}; (**b**) Segregation ratio, $S_R = C_{max}/C_{min}$.

4.4 Effects of the natural convection on the equiaxed dendritic growth

The inevitable gravity-driven natural convection arising from density difference in the liquid usually plays an important role in the microstructure evolution during solidification, by dramatically modifying the transport of heat and solute. In order to study the effects of the gravity-driven natural convection, the equiaxed dendritic growth of the Al-4 wt.% Cu alloy is simulated using the PF model coupled with fluid dynamics equations as ref. [47]. In order to expedite the PF simulation, the vector-valued method [40] is employed here to solve the fluid dynamics equations more efficiently. However, owing to the significant increase in computing amount to solve the polycrystalline PF formula coupled with fluid dynamics equations, only the case of the experiment E2 (Fig. 3~~Fig. 3~~(b)) is considered, in which the cooling rate (R_c = 0.5 K/min) is not very slow and the number of grains is also not too large. It

should be noted that the large-scale 3D PF simulations of dendrite growth with liquid convection have been realized by Zhang et al. [48] and Takaki et al. [49] recently. However, for the present work the size for a 3D computational size is much larger than those studies, and thus here we only perform 2D simulations. Furthermore, the natural convection considered in the present PF simulation is caused only by the solutal effect, without considering the thermal effect. It took about 240 hours using the same computing ~~condition~~configuration as mentioned above until the solid fraction reached 0.5, which was much more time consuming than the corresponding simulation (S2) without convection.

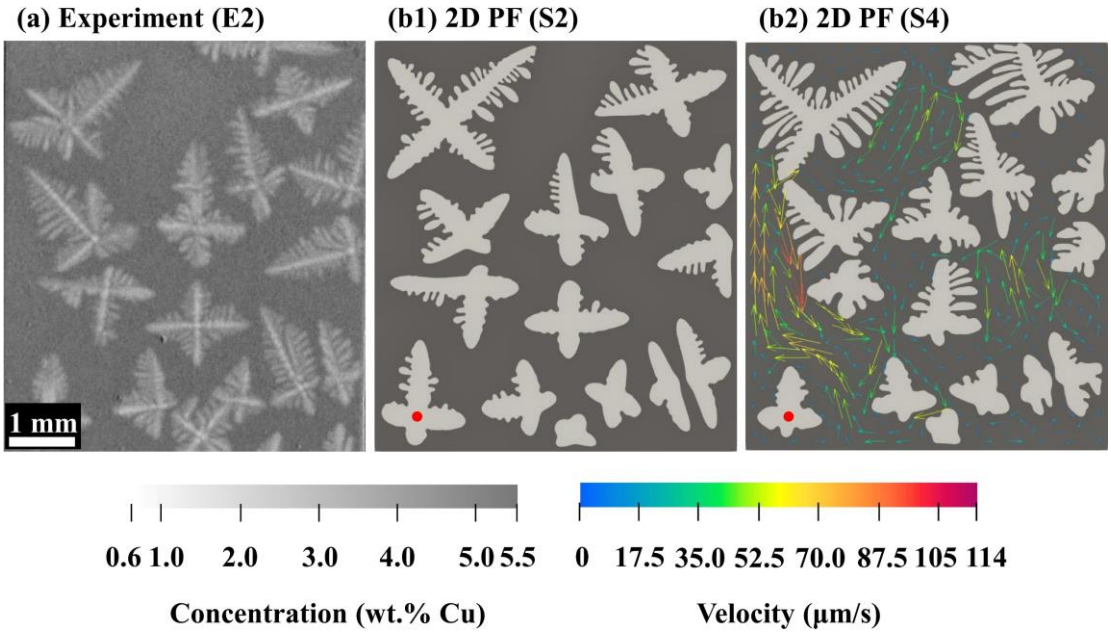

Fig. 8. Equiaxed dendritic morphology in the experiment E2 (**a**) and the 2D PF simulations without (**b1**) and with (**b2**) convection at the same solid fraction f_S = 0.3 in local domains marked by the red boxes in Fig. 1~~Fig. 1~~. In **b1** and **b2**, the grayscale indicates the solute concentration, and the arrows and their colors indicate the liquid flow velocity and its magnitude. The red dots denote the location of the minimum solute concentration in the whole domain.

The simulated equiaxed dendritic microstructure in the 2D PF simulations without and with the natural convection, as well as that in the solidification

experiment, are shown in Fig. 8~~Fig. 8~~. Although the rejected heavier solute copper induces downward flow along the solid-liquid interface, ~~T~~there exists some upward flow in Fig. 8~~Fig. 8~~(b2) due to several flow vortices, which is also clarified in our previous study [50]. Furthermore, in the real solidification experiment E2, several dendrites settle down while they are growing. The settlement arises from the liquid flow and the density difference between solid and liquid. And this phenomenon has also been studied in ref. [50], by modeling of coupled motion and growth of equiaxed dendrite using the PF method. Recently, Sakane et al. [26] also performed 2D large-scale PF lattice Boltzmann simulations of polycrystalline equiaxed solidification with motion of a massive number of dendrites. However, in the present work, the motion of dendrites is not considered in order to expedite the PF simulation. By comparing the shape of each grain in Fig. 8~~Fig. 8~~(b1) (without convection) and Fig. 8~~Fig. 8~~(b2) (with convection), it could be seen that the natural convection has a significant influence on the equiaxed dendritic morphology when grains grow into big size. However, this influence depends on the location and orientation of ~~the~~ a grain. In detail, the growth of the upstream arms will be promoted, while that of the downstream arms will be suppressed, which has been indicated in many previous studies [16, 40, 51]. The influence of dendrite arm orientation with respect to gravity on equiaxed grain growth has been studied in ref. [16]. The authors explained that the different behaviors between the upstream and downstream arms is due to the poisoning effect of arm growth by the solute rejected by the other arms in the adjacent melt. The rejected solute sinks down by gravity as copper is heavier than aluminum. Furthermore, the secondary arms are also affected by the liquid convection. Similar to the primary dendritic arms, the sidebranches at the upstream side are also more developed than those on the downstream side. In order to quantitatively estimate the effect of the liquid convection on the sidebranches, the SDAS in the solidification experiment (E2) and 2D PF simulations (S2 without convection and S4 with convection) are measured, and the results are listed in Table 2~~Table 2~~.

Table 2. Comparison of the average SDAS in the solidification experiment and 2D PF

simulations at the same solid fraction, $f_S = 0.5$.

	Experiment (E2)	Simulation (S2)	Simulation (S4)
SDAS, λ_2 (μm)	118.4 ± 10.15	132.9 ± 13.49	140.9 ± 20.75

As mentioned above, because a much longer time is taken in 2D PF simulations to reach the same solid fraction than that in the experiment (Fig. 5~~Fig. 5~~(a) and Fig. 9~~Fig. 9~~(a)), the coarsening of the sidebranches is more significant, thus leading to a relatively larger SDAS in simulations. The natural convection does not affect this trend apparently. However, it is worth noting that the average SDAS is increased about 6% by convection in the 2D PF simulations, which suggests that the solute convection may promote the overall coarsening of sidebranches during solidification.

The effect of the natural convection on the solid fraction, f_S, is shown in Fig. 9~~Fig. 9~~. In the 2D PF simulations (S2 and S4), f_S is much lower than the experimental data. Besides, Fig. 9~~Fig. 9~~(a) also shows that the natural convection has no obvious influence on f_S at the beginning of solidification (less than 100 s during solidification), but then it slightly affects the solid fraction before $f_S = 0.25$. During this period, f_S is slightly larger when convection is taken into account (S4) than that in the case without convection (S2). Then, no apparent difference can be found between the simulations with and without convection. This evolution behavior denotes that natural convection only takes effect when the solute gradient in liquid at the most of solid-liquid interface is sufficiently high. High concentration gradient results in a relative strong convection, thus leading to a little higher growth rate. Subsequently, as solidification proceeds ($f_S > 0.25$), the convection effect gradually decreases and both f_S become almost identical in PF simulations with and without convection. The variation rate of solid fraction with time, $\Delta f_S/\Delta t$, is plotted in Fig. 9~~Fig. 9~~(b). Also, the influence of convection on $\Delta f_S/\Delta t$ is not obvious, and f_S increases faster in S4 than that in S2 after solidifying for a while. And then during the subsequent stage of solidification ($f_S > 0.25$), the time change rates of the solid fraction in different simulations gradually get identical.

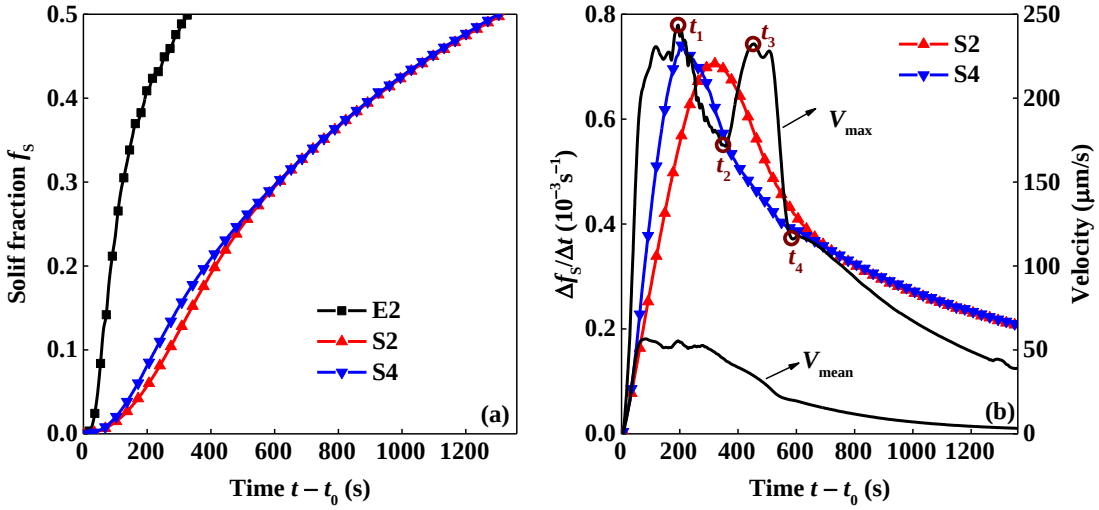

Fig. 9. Effects of gravity-driven natural convection on solid fraction. (**a**) Solid fraction, f_S; (**b**) Variation rate of the solid fraction, $\Delta f_S/\Delta t$, and the maximum and mean flow velocity, V_{max} and V_{mean}.

Interestingly, the maximum and mean flow velocity, V_{max} and V_{mean}, globally vary in a similar manner as the solid fraction variation rate at the beginning of solidification, namely increasing first and then decreasing, as shown in Fig. 9~~Fig. 9~~(b). The solute concentration and liquid flow velocity at time t_1 to t_4 marked by circles in Fig. 9~~Fig. 9~~(b) are shown in Fig. 10~~Fig. 10~~. During the early solidification stage ($t < t_1$) when the grains are isolated from their neighbors, with grains growing faster and faster, more and more solute is rejected into the liquid phase, leading to large solute variations in the melt. Consequently, the liquid flow is promoted until V_{max} reaches the peak value at t_1. Then, with $\Delta f_S/\Delta t$ decreasing, V_{max} also declines because less solute is rejected into liquid, and V_{max} appears in the interdendritic liquid channel at time t_2. As solidification proceeds, the rejected solute in liquid begins to homogenize because of the lower phase transformation rate, and the reduced solute gradient in the liquid ahead of the solid-liquid interface also contributes to weaking the solutal natural convection.

In addition, apparent oscillations are observed for V_{max}, which may be attributed to the complicated flow pattern caused by the developed dendrites. As impinged

growth takes place among grains, the liquid channel between two grains becomes more and more narrow, and the enlarged flow pressure makes V_{max} increase again from t_2 to t_3. Whereafter, V_{max} starts to decrease since the liquid channel is too narrow and the liquid flow nearby are very weak, which could not render sufficient pressure to drive the liquid pass through the narrow channel. When the solid fraction becomes higher and higher, all grains are impinged with each other. Meanwhile, the solute gradient in liquid is reduced and the density contrast is not sharp sufficiently to drive intensive convection. As a result, the solute convection weakens as demonstrated by the reduced mean flow velocity. Until time t_4, V_{max} reappears outside the liquid channel between primary tips and again varies in the same manner as $\Delta f_S/\Delta t$. Compared with the apparently oscillating maximum liquid flow velocity, the variation of the average liquid flow velocity is much more moderate and evolves similarly to the variation rate of solid fraction.

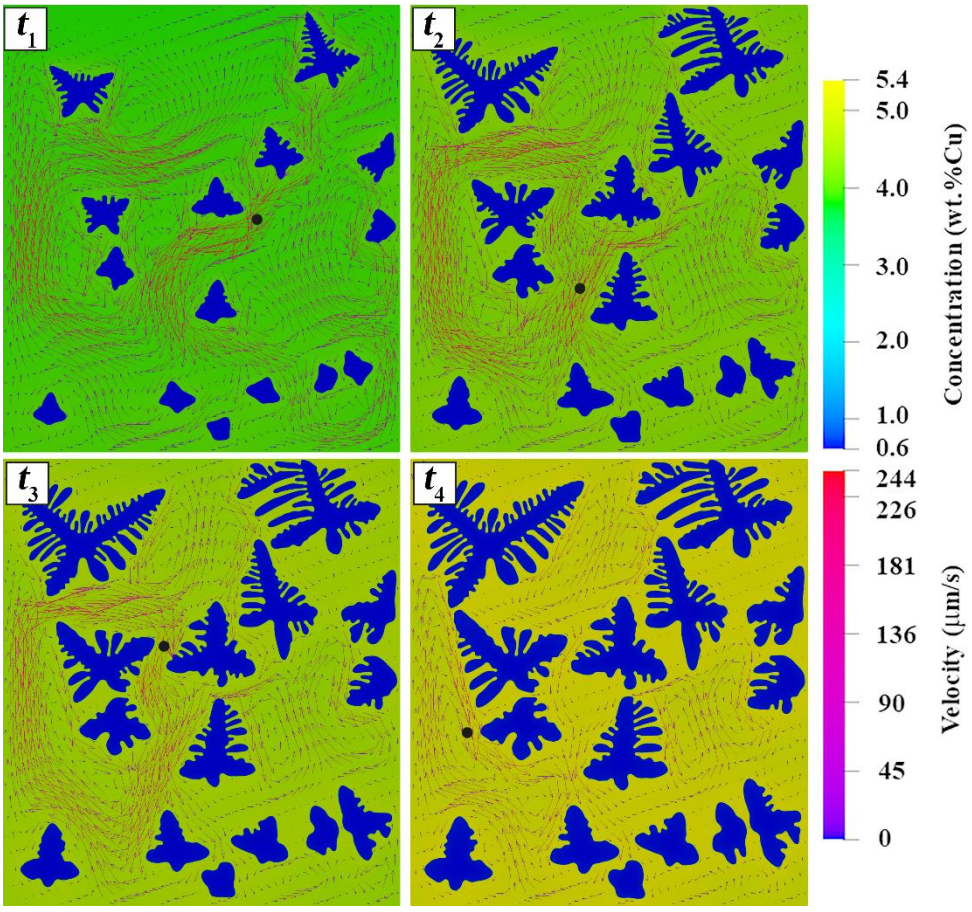

Fig. 10. Solute concentration and liquid flow velocity at the time t_1 to t_4 marked by

the circles in Fig. 9~~Fig. 9~~(b). The time at t_1 to t_4 is 194 s, 349 s, 452 s, and 583 s, respectively.

Moreover, the maximum and minimum solute concentration during solidification in the 2D PF simulations (S2 and S4) are plotted in Fig. 11~~Fig. 11~~(a). It is revealed that the gravity-driven natural convection has no influence on C_{max} which is approximately equal to the equilibrium concentration. However, C_{min} in S4 is slightly larger than that in S2 when the applied undercooling $\Delta T > 6$ K. As indicated by the red dots in Fig. 8~~Fig. 8~~, the grid point with the minimum solute concentration is located at the center of the grain in the bottom-left corner of the computational domain. Since the solute copper element is heavier than the solvent aluminum element, the liquid flows downward, making a large amount solute accumulate surrounding the grains in the bottom region of the computational domain in simulation. Consequently, for the grain with the minimum solute concentration, the post-solidified solid phase has a higher solute concentration, resulting in a higher C_{min} at its center by diffusion in the solid phase. Therefore, the segregation ratio, $S_R = C_{max}/C_{min}$, is smaller in S4 than that in S2 when $\Delta T > 6$ K as shown in Fig. 11~~Fig. 11~~(b), due to the nearly same C_{max} but larger C_{min}.

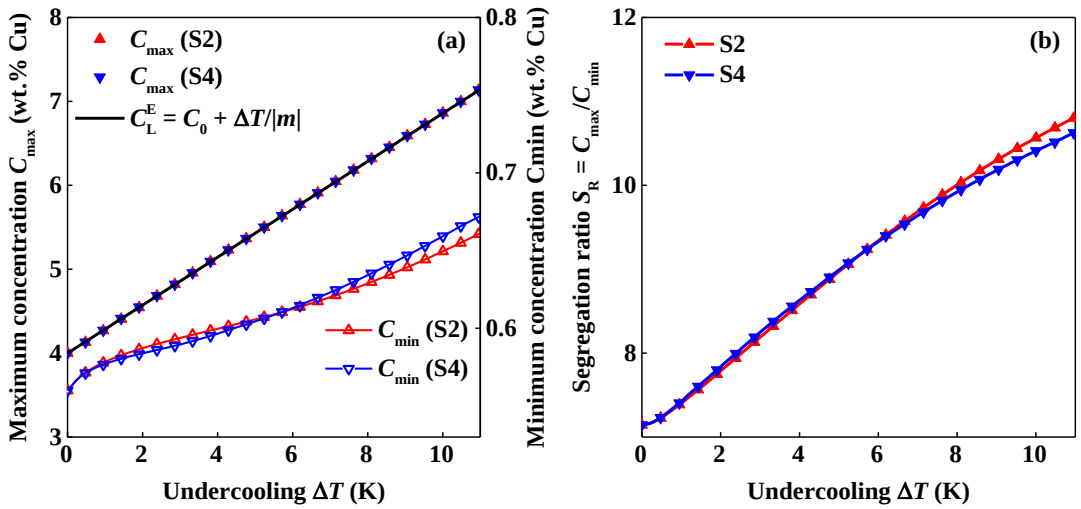

Fig. 11. Effects of liquid gravity-driven natural convection on solute segregation. (**a**) Maximum and minimum solute concentration, C_{max} and C_{min}; (**b**) Solute segregation ratio, $S_R = C_{max}/C_{min}$.

5. Conclusions and outlook

In the present paper, the equiaxed dendritic growth of Al-4 wt.% Cu alloys during polycrystalline solidification under continuous cooling conditions is studied using the in situ and real-time observation of experiments by synchrotron X-ray radiography and large-scale quantitative 2D PF simulations. It is revealed that the equiaxed dendritic morphology and the SDAS in the 2D PF simulations are both in reasonably good quantitative agreement with those in the experiments. With the cooling rate increasing, the SDAS will be reduced as a power function of the cooling rate, which is consistent with the Kattamis-Flemings model. The gravity-driven natural convection will slightly increase the SDAS in the 2D PF simulation.

Moreover, in both of the experiments and 2D PF simulations, the solid fraction evolves with time in the same manner as the JMAK equation, namely $f_S = 1 - \exp[-(kt)^n]$. The parameter k can be fitted well as a linear function of the cooling rate, and another parameter n is approximately a constant that relates to the parabolic growth controlled by diffusion for slow solidification, and the site saturation nucleation in the PF simulations or the continuous nucleation in the real solidification experiments. From the quantitative perspective, at the same solidification time (or undercooling), the solid fraction in the 2D PF simulations is much lower than that in the experiments, and the two fitting parameters, k and n, in the JMAK equation are respectively smaller and larger than the experimental values. Simulations with natural convection show that the flow strength increases with the solute segregation in melt, but has a slight effect on solid fraction only when the severe solute gradient is generated around most of the solid-liquid interface.

Furthermore, the maximum solute concentration in the interdendritic liquid is nearly the same as the equilibrium concentration, which depends on the undercooling rather than the cooling rate. While the minimum solute concentration in the center of a grain is smaller with a larger cooling rate, owing to the shorter time for solute diffusion in the solid phase. The almost same C_{max} in liquid and the smaller C_{min} with a larger cooling rate in solid result in a larger segregation, $S_R = C_{max}/C_{min}$. The liquid

natural convection has no effect on C_{max}, but slightly enhances C_{min} due to the solute segregation induced by melt convection, thus leading to a smaller S_R.

Owing to the significant differences in mass and heat transport behavior between 2D PF simualtions and experimental data, large-scale quantitative 3D PF simulations of multi-dendrite growth during solidification will be considered in our future work. Moreover, the effects of the nucleation undercooling on dendritic growth should be also concerned, so that the PF simulations can exactly reproduce the multi-dendrite growth in the solidification experiments, leading to quantitatively good agreement with the experiments as much as possible.

Acknowledgement

This work was supported by the Youth Innovation Promotion Association CAS, the Science Challenge Project (Grant No. TZ2016004), the Special Scientific Projects of Inner Mongolia, and French National Space Center (CNES), Convention N°174800/00.

Data Availability

The raw/processed data required to reproduce these findings cannot be shared at this time as the data also forms part of an ongoing study.

References

[1] W. Kurz, D. J. Fisher, R. Trivedi, Progress in modelling solidification microstructures in metals and alloys: dendrites and cells from 1700 to 2000, Int. Mater. Rev. 64 (2019) 311-354.

[2] W. Kurz, M. Rappaz, R. Trivedi, Progress in modelling solidification microstructures in metals and alloys. Part II: dendrites from 2001 to 2018, Int. Mater. Rev. (2020) 47.

[3] P. Pelce, Y. Pomeau, Dendrites in the small undercooling limit, Stud. Appl. Math. 74 (1986) 245-258.

[4] G. Ivantsov, Temperature field around a spherical, cylindrical, and needle-shaped

crystal, growing in a pre-cooled melt Dok. Akad. Nauk SSSR 1 (1947) 567-569.

[5] J. Lipton, M. E. Glicksman, W. Kurz, Dendritic growth into undercooled alloy melts, Materials Science and Engineering 65 (1984) 57-63.

[6] J. Lipton, M. E. Glicksman, W. Kurz, Equiaxed dendrite growth in alloys at small supercooling, Metall. Trans. A 18 (1987) 341-345.

[7] M. Benamar, P. Bouissou, P. Pelce, An exact solution for the shape of a crystal growing in a forced flow, Journal of Crystal Growth 92 (1988) 97-100.

[8] P. Bouissou, P. Pelcé, Effect of a forced flow on dendritic growth, Physical Review A 40 (1989) 6673-6680.

[9] C. Y. Wang, C. Beckermann, Equiaxed dendritic solidification with convection: Part I. Multiscale/multiphase modeling, Metall. Mater. Trans. A 27 (1996) 2754-2764.

[10] C. A. Gandin, G. Guillemot, B. Appolaire, N. T. Niane, Boundary layer correlation for dendrite tip growth with fluid flow, Mater. Sci. Eng. A 342 (2003) 44-50.

[11] R. Ananth, W. N. Gill, Self-consistent theory of dendritic growth with convection, Journal of Crystal Growth 108 (1991) 173-189.

[12] C. Beckermann, C. Y. Wang, Equiaxed dendritic solidification with convection: Part III. Comparisons with NH4Cl-H2O experiments, Metall. Mater. Trans. A 27 (1996) 2784-2795.

[13] Q. Li, C. Beckermann, Modeling of free dendritic growth of succinonitrile–acetone alloys with thermosolutal melt convection, Journal of Crystal Growth 236 (2002) 482-498.

[14] A. Karma, D. Tourret, Atomistic to continuum modeling of solidification microstructures, Curr. Opin. Solid St. M. 20 (2016) 25-36.

[15] S. Akamatsu, H. Nguyen-Thi, In situ observation of solidification patterns in diffusive conditions, Acta Mater. 108 (2016) 325-346.

[16] A. Bogno, H. Nguyen-Thi, G. Reinhart, B. Billia, J. Baruchel, Growth and interaction of dendritic equiaxed grains: In situ characterization by synchrotron X-ray radiography, Acta Mater. 61 (2013) 1303-1315.

[17] M. Becker, S. Klein, F. Kargl, Free dendritic tip growth velocities measured in

Al-Ge, Phys. Rev. Mater. 2 (2018) 6.

[18] Y. Chen, D. Z. Li, B. Billia, H. Nguyen-Thi, X. B. Qi, N. M. Xiao, Quantitative Phase-field Simulation of Dendritic Equiaxed Growth and Comparison with in Situ Observation on Al-4 wt.% Cu Alloy by Means of Synchrotron X-ray Radiography, ISIJ Int. 54 (2014) 445-451.

[19] X. B. Qi, Y. Chen, X. H. Kang, D. Z. Li, The Effect of Natural Convection on Equiaxed Dendritic Growth: Quantitative Phase-Field Simulation and Comparison with Synchrotron X-Ray Radiography Monitoring Data, Adv. Mater. Sci. Eng. (2016) 10.

[20] A. K. Boukellal, J.-M. Debierre, G. Reinhart, H. Nguyen-Thi, Scaling laws governing the growth and interaction of equiaxed Al-Cu dendrites: A study combining experiments with phase-field simulations, Materialia 1 (2018) 62-69.

[21] A. G. Murphy, R. H. Mathiesen, Y. Houltz, J. Li, C. Lockowandt, K. Henriksson, G. Zimmermann, N. Melville, D. J. Browne, XRMON-SOL: Isothermal equiaxed solidification of a grain refined Al–20wt%Cu alloy, Journal of Crystal Growth 440 (2016) 38-46.

[22] Y. Souhar, V. F. De Felice, C. Beckermann, H. Combeau, M. Založnik, Three-dimensional mesoscopic modeling of equiaxed dendritic solidification of a binary alloy, Comput. Mater. Sci. 112 (2016) 304-317.

[23] A. Olmedilla, M. Zaloznik, H. Combeau, Quantitative 3D mesoscopic modeling of grain interactions during equiaxed dendritic solidification in a thin sample, Acta Mater. 173 (2019) 249-261.

[24] T. Takaki, S. Sakane, M. Ohno, Y. Shibuta, T. Shimokawabe, T. Aoki, Primary arm array during directional solidification of a single-crystal binary alloy: Large-scale phase-field study, Acta Mater. 118 (2016) 230-243.

[25] T. Z. Gong, Y. Chen, Y. F. Cao, X. H. Kang, D. Z. Li, Fast simulations of a large number of crystals growth in centimeter-scale during alloy solidification via nonlinearly preconditioned quantitative phase-field formula, Comput. Mater. Sci. 147 (2018) 338-352.

[26] S. Sakane, T. Takaki, M. Ohno, Y. Shibuta, T. Aoki, Two-dimensional large-scale

phase-field lattice Boltzmann simulation of polycrystalline equiaxed solidification with motion of a massive number of dendrites, Comput. Mater. Sci. 178 (2020) 109639.

[27] A. Buffet, H. N. Thi, A. Bogno, T. Schenk, N. Mangelinck-Noel, G. Reinhart, N. Bergeon, B. Billia, J. Baruchel, Materials Science Forum 649 (2010) 331-336.

[28] B. Echebarria, R. Folch, A. Karma, M. Plapp, Quantitative phase-field model of alloy solidification, Phys. Rev. E 70 (2004) 061604.

[29] Y. Chen, A.-A. Bogno, N. M. Xiao, B. Billia, X. H. Kang, H. Nguyen-Thi, X. H. Luo, D. Z. Li, Quantitatively comparing phase-field modeling with direct real time observation by synchrotron X-ray radiography of the initial transient during directional solidification of an Al–Cu alloy, Acta Mater. 60 (2012) 199-207.

[30] Y. Chen, B. Billia, D. Z. Li, H. Nguyen-Thi, N. M. Xiao, A. A. Bogno, Tip-splitting instability and transition to seaweed growth during alloy solidification in anisotropically preferred growth direction, Acta Mater. 66 (2014) 219-231.

[31] A. J. Clarke, D. Tourret, Y. Song, S. D. Imhoff, P. J. Gibbs, J. W. Gibbs, K. Fezzaa, A. Karma, Microstructure selection in thin-sample directional solidification of an Al-Cu alloy: In situ X-ray imaging and phase-field simulations, Acta Mater. 129 (2017) 203-216.

[32] A. Karma, Phase-field formulation for quantitative modeling of alloy solidification, Phys. Rev. Lett. 87 (2001) 115701.

[33] K. Glasner, Nonlinear Preconditioning for Diffuse Interfaces, Journal of Computational Physics 174 (2001) 695-711.

[34] W. Bangerth, D. Davydov, T. Heister, L. Heltai, G. Kanschat, M. Kronbichler, M. Maier, B. Turcksin, D. Wells, The deal.II Library, Version 8.4, J. Numer. Math. 24 (2016) 135-141.

[35] C. Y. Wang, C. Beckermann, Equiaxed dendritic solidification with convection: Part II. Numerical simulations for an Al-4 Wt pct Cu alloy, Metall. Mater. Trans. A 27 (1996) 2765-2783.

[36] M. Rebow, D. J. Browne, On the dendritic tip stability parameter for aluminium alloy solidification, Scripta Materialia 56 (2007) 481-484.

[37] J.-H. Lee, S. Liu, H. Miyahara, R. Trivedi, Diffusion-coefficient measurements in liquid metallic alloys, Metall. Mater. Trans. B 35 (2004) 909-917.

[38] M. Gündüz, J. D. Hunt, The measurement of solid-liquid surface energies in the Al-Cu, Al-Si and Pb-Sn systems, Acta Metallurgica 33 (1985) 1651-1672.

[39] S. Liu, R. E. Napolitano, R. Trivedi, Measurement of anisotropy of crystal-melt interfacial energy for a binary Al–Cu alloy, Acta Mater. 49 (2001) 4271-4276.

[40] T. Z. Gong, Y. Chen, D. Z. Li, Y. F. Cao, P. X. Fu, Quantitative comparison of dendritic growth under forced flow between 2D and 3D phase-field simulation, Int. J. Heat Mass Transf. 135 (2019) 262-273.

[41] W. U. Mirihanage, K. V. Falch, D. Casari, S. McFadden, D. J. Browne, I. Snigireva, A. Snigirev, Y. J. Li, R. H. Mathiesen, Non-steady 3D dendrite tip growth under diffusive and weakly convective conditions, Materialia 5 (2019) 100215.

[42] M. C. Flemings, Coarsening in solidification processing, Mater. Trans. 46 (2005) 895-900.

[43] M. Avrami, Kinetics of phase change I - General theory, Journal of Chemical Physics 7 (1939) 1103-1112.

[44] M. Avrami, Kinetics of Phase Change. II Transformation-Time Relations for Random Distribution of Nuclei, The Journal of Chemical Physics 8 (1940) 212-224.

[45] M. Avrami, Granulation, Phase Change, and Microstructure - Kinetics of Phase Change. III, Journal of Chemical Physics 9 (1941) 177-184.

[46] T. Gong, Y. Chen, S. Li, Y. Cao, D. Li, X.-Q. Chen, G. Reinhart, H. Nguyen-Thi, Revisiting dynamics and models of microsegregation during polycrystalline solidification of binary alloy, J. Mater. Sci. Technol. 74 (2021) 155-167.

[47] H.-J. D. C. Beckermann, I. Steinbacn, A. Karma, X. Tong, Modeling melt convection in phase-field simulation of solidification, Journal of Computational Physics 154 (1999) 29.

[48] A. Zhang, S. Meng, Z. Guo, J. Du, Q. Wang, S. Xiong, Dendritic Growth Under Natural and Forced Convection in Al-Cu Alloys: From Equiaxed to Columnar Dendrites and from 2D to 3D Phase-Field Simulations, Metall. Mater. Trans. B-Proc. Metall. Mater. Proc. Sci. 50 (2019) 1514-1526.

[49] T. Takaki, S. Sakane, M. Ohno, Y. Shibuta, T. Aoki, Large–scale phase–field lattice Boltzmann study on the effects of natural convection on dendrite morphology formed during directional solidification of a binary alloy, Comput. Mater. Sci. 171 (2020) 109209.

[50] X. B. Qi, Y. Chen, X. H. Kang, D. Z. Li, T. Z. Gong, Modeling of coupled motion and growth interaction of equiaxed dendritic crystals in a binary alloy during solidification, Sci Rep 7 (2017) 16.

[51] S. Sakane, T. Takaki, R. Rojas, M. Ohno, Y. Shibuta, T. Shimokawabe, T. Aoki, Multi-GPUs parallel computation of dendrite growth in forced convection using the phase-field-lattice Boltzmann model, Journal of Crystal Growth 474 (2017) 154-159.